



Publication Year	2015
Acceptance in OA @INAF	2020-03-31T08:44:25Z
Title	New Signatures of the Milky Way Formation in the Local Halo and Inner-halo Streamers in the Era of Gaia
Authors	RE FIORENTIN, Paola; LATTANZI, Mario G.; SPAGNA, Alessandro; CURIR, Anna
DOI	10.1088/0004-6256/150/4/128
Handle	http://hdl.handle.net/20.500.12386/23736
Journal	THE ASTRONOMICAL JOURNAL
Number	150

NEW SIGNATURES OF THE MILKY WAY FORMATION IN THE LOCAL HALO AND INNER-HALO STREAMERS IN THE ERA OF GAIA

PAOLA RE FIORENTIN¹, MARIO G. LATTANZI^{1,2}, ALESSANDRO SPAGNA¹, AND ANNA CURIR¹
¹INAF—Osservatorio Astrofisico di Torino, Strada Osservatorio 20, I-10025 Pino Torinese (TO), Italy; re_florentin@oato.inaf.it
²Shanghai Astronomical Observatory, Chinese Academy of Sciences, 80 Nandan Road, 200030 Shanghai, China
 Received 2015 February 26; accepted 2015 August 8; published 2015 September 30

ABSTRACT

We explore the vicinity of the Milky Way through the use of spectrophotometric data from the Sloan Digital Sky Survey and high-quality proper motions derived from multi-epoch positions extracted from the Guide Star Catalog II database. In order to identify and characterize streams as relics of the Milky Way formation, we start with classifying, selecting, and studying 2417 subdwarfs with $[\text{Fe}/\text{H}] < -1.5$ up to 3 kpc away from the Sun as tracers of the local halo system. Then, through phase-space analysis, we find statistical evidence of five discrete kinematic overdensities among 67 of the fastest-moving stars and compare them to high-resolution N -body simulations of the interaction between a Milky Way–like galaxy and orbiting dwarf galaxies with four representative cases of merging histories. The observed overdensities can be interpreted as fossil substructures consisting of streamers torn from their progenitors; such progenitors appear to be satellites on prograde and retrograde orbits on different inclinations. In particular, of the five detected overdensities, two appear to be associated, yielding 21 additional main-sequence members, with the stream of Helmi et al. that our analysis confirms is on a high-inclination prograde orbit. The three newly identified kinematic groups could be associated with the retrograde streams detected by Dinescu and Kewley et al.; whatever their origin, the progenitor(s) would be on retrograde orbit(s) and inclination(s) within the range $10^\circ \div 60^\circ$. Finally, we use our simulations to investigate the impact of observational errors and compare the current picture to the promising prospect of highly improved data expected from the *Gaia* mission.

Key words: Galaxy: formation – Galaxy: halo – Galaxy: kinematics and dynamics

1. INTRODUCTION

The formation and evolution of galaxies is one of the outstanding problems in astrophysics, one which can be profitably engaged directly through detailed study of our own Galaxy, the Milky Way (e.g., Freeman & Bland-Hawthorn 2002; Helmi 2008).

In the context of hierarchical structure formation, galaxies such as the Milky Way grow by mergers and accretion of smaller systems, perhaps similar to what are now observed as dwarf galaxies. These satellite galaxies—torn apart by the tidal gravitational field of the parent galaxy—are progressively disrupted, giving rise to trails of stellar debris streams along their orbits, spatial signatures that eventually disappear due to dynamical mixing. After the accretion era ends, a spheroidal halolike component is left from their collective assembly (e.g., Searle & Zinn 1978; Bullock & Johnston 2005; Abadi et al. 2006; Moore et al. 2006; Sales et al. 2007; De Lucia 2012).

Of all the Galactic components, it is indeed the stellar halo that offers the best opportunity for probing details of the merging history of the Milky Way (see, e.g., Helmi 2008). Past explorations have demonstrated that there is a concrete possibility of identifying groups of halo stars that originate from common progenitor satellites (Eggen 1977; Ibata et al. 1994, 2003; Majewski et al. 1996; Helmi et al. 1999; Chiba & Beers 2000; Dinescu 2002; Kewley et al. 2007; Klement et al. 2009; Morrison et al. 2009; Schlafman et al. 2009; Smith et al. 2009; Duffau et al. 2014).

Simulations show that a Milky Way mass galaxy within a Λ CDM universe will have halo stars associated with substructures and streams (e.g., Johnston 1998; Harding et al. 2001; Starkenburg et al. 2009; Helmi et al. 2011; Gomez

et al. 2013). These substructures, much like those seen in the halo system of the Milky Way, are sensitive to recent (within the last 8 Gyr) merging events and are more prominent in the outer region of the halo (galactocentric radii beyond 15–20 kpc), whereas the inner-halo region appears significantly smoother.

Based on data from the SEGUE spectroscopic survey, Schlafman et al. (2009) found that metal-poor main-sequence turnoff stars in the inner-halo region of the Milky Way (within ~ 20 kpc from the Sun) exhibit clear evidence for radial velocity clustering on small spatial scales (they refer to these as ECHOS for Elements of Cold Halo Substructure). They estimated that about 10% of the inner-halo turnoff stars belong to ECHOS and inferred the existence of about 1000 ECHOS in the entire inner-halo volume. Schlafman et al. (2011) suggest that the most likely progenitors of ECHOS are dwarf spheroidal galaxies with masses on the order of $10^9 M_\odot$.

In the solar neighborhood, up to 1–2 kpc of the Sun, stellar streams have also been discovered as overdensities in the phase-space distribution of stars, integrals of motion, and action-angle variables (see Klement 2010 for a review). Prominent examples are the two stellar debris streams in the halo population passing close to the Sun detected by Helmi et al. (1999) when combining high-quality *Hipparcos* proper motions with ground-based observations. Formed via destruction of a satellite whose debris now occupy the inner-halo region with no apparent spatial structure, these streamers retain very similar velocities and are seen as clumps in angular momentum space where stars from a common progenitor appear rather confined (Helmi & de Zeeuw 2000).

Besides the Helmi stream, ω Centauri (Dinescu 2002; Majewski et al. 2012), and the Kapteyn and Arcturus (e.g.,

Eggen 1971) streams, Klement (2010) lists a few other halo substructures found in the solar neighborhood: these are still small numbers compared to the few hundred streams expected (i.e., 300–500; Helmi & White 1999; Gould 2003). Actually, recovering fossil structures in the inner halo is considerably more difficult, as strong phase-mixing takes place. This degeneracy can only be broken with 6D (phase-space) or 7D (including abundances) information achievable by integrating astrometry, photometry, and spectroscopy.

The SDSS–GSC II Kinematic Survey (SGKS) that we exploit here was produced to serve this task (see Spagna et al. 2010b). In the future, new ground- and space-based surveys such as *Gaia* (e.g., Perryman et al. 2001; Turon et al. 2005), *Gaia* ESO Survey (GES; Gilmore et al. 2012), and LAMOST (Zhao et al. 2012) will provide high-precision data that will usher us in a new era of Milky Way studies.

In Section 2, we introduce the data used to isolate a sample of nearby halo subdwarfs from the SGKS catalog. The kinematic and orbital properties of the local halo subdwarf population are discussed in Section 3, where we present algorithms to search for kinematic substructures, recovering known streams (Helmi et al. 1999; Dinescu 2002; Kepley et al. 2007), as well as new kinematic overdensities. In Section 4, we present the high-resolution N -body numerical simulations of four minor mergers used to study galaxy interactions and the properties of accretion events in the vicinity of the Sun. In Section 5, we investigate the impact of observational errors resulting from current ground-based data and from high accurate data expected from the *Gaia* satellite. Finally, in Section 6, we compare observations to these numerical simulations and infer the nature of the detected fast-moving groups.

2. THE SDSS–GSC II KINEMATIC SURVEY (SGKS)

This study is based on a new kinematic catalog, derived by assembling spectrophotometric stellar data from the Seventh Data Release of the Sloan Digital Sky Survey (SDSS DR7; Abazajian et al. 2010), which included data from the Sloan Extension for Galactic Understanding and Exploration (SEGUE; Yanny et al. 2009), supplemented by astrometric parameters extracted from the database used for the construction of the Second Guide Star Catalog (GSC II; Lasker et al. 2008). This SDSS–GSC II catalog contains positions, proper motions, classification, and *ugriz* photometry for 77 million sources down to $r \sim 20$, over 9000 square degrees.

Proper motions are computed by combining multi-epoch positions from SDSS DR7 and the GSC II database; typically, 5–10 observations are available for each source, spanning up to 50 years. The typical formal errors on those proper motions are in the range 2–3 mas yr⁻¹ per coordinate for $16 < r < 18.5$, comparable to the internal precision of the SDSS proper motions computed by Munn et al. (2008). Although much of the photographic material (Schmidt plates) used to derive the first epoch information is in common with that used by Munn et al. (2008), who employed data from the USNO-B project, the plate digitization and measurement processes and the calibration methods that led to the first epoch positions were somewhat different. Of particular relevance is the minimization of systematic errors that can affect proper-motion accuracy, a true driver in analysis like those conducted in this study. An accurate validation of our proper motions was discussed in Spagna et al. (2010a).

Radial velocities and astrophysical parameters are available for about 151,000 sources cross-matched with the SDSS spectroscopic catalog. Typical accuracy is of 5–10 km s⁻¹ in line of sight velocity; 250 K in effective temperature, T_{eff} ; 0.25 dex in surface gravity, $\log g$; and 0.20 dex in metallicity, $[\text{Fe}/\text{H}]$, as estimated within the SEGUE Spectral Parameter Pipeline (SSPP; i.e., Re Fiorentin et al. 2007; Allende Prieto et al. 2008; Lee et al. 2008a, 2008b). We specify that the sample includes only objects with no problems related to the spectrum and classified without any cautionary flag by the SSPP. In the case of multiple spectra, we take the spectrum with the highest signal-to-noise ratio (S/N).

From the SDSS–GSC II catalog, we select as tracers sources with $4500 \text{ K} < T_{\text{eff}} < 7500 \text{ K}$ and $\log g > 3.5$, corresponding to FGK dwarfs.

The observed magnitudes are corrected for interstellar absorption via the extinction maps of Schlegel et al. (1998), based on the 6' resolution COBE/DIRBE dust map, that we preferred to the more recent, but of inferior resolution (7'–14'), reddening maps published by Schlafly et al. (2014). Then, we transformed the $E(B - V)$ to the SDSS photometric system by adopting the extinction ratio $A_r/A_V = 0.875$ (from Table 1 of Girardi et al. 2004) that is appropriate for our FGK dwarf sample.

Photometric distances good to $\sigma_d/d \sim 20\%$ are computed by means of the photometric parallax relation established for FGK main-sequence stars by Ivezić et al. (2008). Here, the metallicity-dependent absolute magnitude relations, $M_r = f(g - i, [\text{Fe}/\text{H}])$, use the spectroscopic $[\text{Fe}/\text{H}]$ instead of the photometric metallicity adopted by Ivezić et al. (2008). We also apply the additional color thresholds from Klement et al. (2009) in order to remove turnoff stars, whose estimated M_r may be affected by residual systematic errors.

Galactic space-velocity components³ are estimated under the assumption that the Sun is at a distance of 8 kpc from the center of the Milky Way, the LSR rotates at 220 km s⁻¹ about the Galactic center, and the peculiar velocity of the Sun relative to the LSR is $(U, V, W)_\odot = (10.00, 5.25, 7.17) \text{ km s}^{-1}$ (Dehnen & Binney 1998).

Finally, in order to minimize the effect of outliers (e.g., mismatches, blends, and sources with low S/N) and therefore obtain a sample with accurate distance and kinematics suitable for our stellar stream search, we impose a threshold on proper-motion errors ($< 10 \text{ mas yr}^{-1}$ per component), constrain magnitudes to the range $13.5 < g < 20.5$, limit the errors on the derived velocity components to better than 50 km s⁻¹, and remove total space velocities above 600 km s⁻¹. These are the properties of the 24,634 stars listed in the SGKS catalog.

3. DATA ANALYSIS

Among the full sample of FGK dwarfs from the SGKS catalog, we have selected specific sub-samples of tracers of the Galactic halo population in the inner-halo region and analyzed their phase-space distribution.

Here, we focus on a sample of 2417 metal-poor stars ($[\text{Fe}/\text{H}] < -1.5$) outside the Galactic plane ($|z| > 1 \text{ kpc}$) and located within 3 kpc of the Sun. Within this volume, the selected sample has median errors on U , V , and W of 12, 13,

³ Throughout this work, U , V , and W indicate Galactic velocity components relative to the LSR and follow the convention with U positive toward the Galactic center, V positive in the direction of Galactic rotation, and $W > 0$ toward the North Galactic Pole.

Table 1
Halo Velocity Parameters

$\langle U \rangle$ (km s ⁻¹)	$\langle V + 220 \rangle$ (km s ⁻¹)	$\langle W \rangle$ (km s ⁻¹)	σ_U (km s ⁻¹)	σ_V (km s ⁻¹)	σ_W (km s ⁻¹)	ρ_{UV}	ρ_{UV}	ρ_{VW}
15 ± 2	25 ± 2	-4 ± 2	126 ± 1	100 ± 1	91 ± 1	-0.09 ± 0.02	-0.18 ± 0.02	0.05 ± 0.02

Notes. The Milky Way halo velocity parameters as determined from our selected sample of 2417 FGK subdwarfs. The table lists mean velocities, dispersions, and corresponding correlation coefficients in Galactic coordinates. The correlation between U and W is noticeable (see the text).

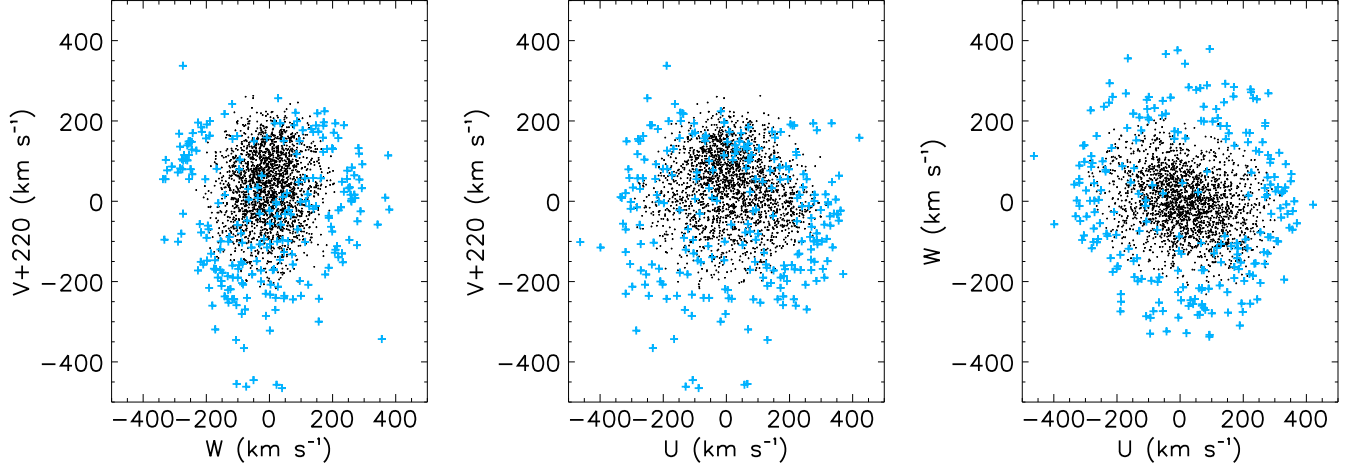


Figure 1. Distribution of nearby halo stars in velocity space for our selected sample of 2417 FGK subdwarfs, with $[\text{Fe}/\text{H}] < -1.5$ and $|z| > 1$ kpc within 3 kpc of the Sun. The 10% fastest-moving stars (242) are marked as crosses.

and 9 km s^{-1} , respectively; this results in errors in the velocity difference between stellar pairs that do not exceed $\sim 20 \text{ km s}^{-1}$. Such a value is suited for careful investigations of substructure, as the kinematic analysis presented below will show.

3.1. Local Halo Velocity Distribution

From the selected sample, we measure the mean velocities ($\langle U \rangle$, $\langle V + 220 \rangle$, $\langle W \rangle$), the velocity ellipsoid (σ_U , σ_V , σ_W), and the correlations among velocity components (ρ_{UV} , ρ_{UV} , ρ_{VW}) as reported in Table 1.

The kinematic properties of the selected tracers are representative of the halo population in the vicinity of the Sun (e.g., Chiba & Beers 2000).

The significant correlation $\rho_{UV} = -0.18 \pm 0.02$ between the radial and vertical velocity components indicates a tilt of the velocity ellipsoid (Figure 1, right panel).

Using the tilt formula (see, e.g., Binney & Merrifield 1998)

$$\tan 2\delta_{UV} = \frac{2\sigma_{UV}^2}{\sigma_U^2 - \sigma_V^2} = \frac{2\rho_{UV}\sigma_U\sigma_V}{\sigma_U^2 - \sigma_V^2}, \quad (1)$$

and the values in Table 1 for the correlation coefficient and velocity dispersions along the U and W axes, we derive a tilt angle of $\delta_{UV} = -14^\circ 5' \pm 1^\circ 4'$, revealing that the (U, W) distribution points toward the Galactic center.

In fact, for our halo sample of 2417 FGK subdwarfs with $\langle z \rangle \approx 1.2$ kpc and $\langle R \rangle \approx 8.3$ kpc, we estimate a mean position angle $\langle \tan^{-1}(z/R) \rangle \approx 8^\circ 3'$. This result is fairly consistent with the tilting effects on the velocity ellipsoids due to the gravitational potential produced by the stellar disk and dark matter halo (Bond et al. 2010 and references therein). We also measure smaller but statistically significant correlations in the (U, V) and (V, W) velocity planes.

In the following, we look for halo streamers in the high-velocity tail of the (U, V, W) velocity distribution, where kinematic substructures are more easily detected. In order to select high-velocity stars, we model the velocity distribution as a tilted Schwarzschild ellipsoid:

$$f(U, V, W) = \text{const} \cdot e^{-\frac{1}{2}E(U, V, W)}, \quad (2)$$

where E is the velocity function defined by

$$\begin{aligned} E(U, V, W) &= \frac{R_{UU}}{R} \left(\frac{U - \langle U \rangle}{\sigma_U} \right)^2 + \\ & \frac{R_{VV}}{R} \left(\frac{V - \langle V \rangle}{\sigma_V} \right)^2 + \frac{R_{WW}}{R} \left(\frac{W - \langle W \rangle}{\sigma_W} \right)^2 + \\ & 2 \frac{R_{UV}}{R} \left(\frac{U - \langle U \rangle}{\sigma_U} \right) \left(\frac{V - \langle V \rangle}{\sigma_V} \right) + \\ & 2 \frac{R_{VW}}{R} \left(\frac{V - \langle V \rangle}{\sigma_V} \right) \left(\frac{W - \langle W \rangle}{\sigma_W} \right) + \\ & 2 \frac{R_{UW}}{R} \left(\frac{U - \langle U \rangle}{\sigma_U} \right) \left(\frac{W - \langle W \rangle}{\sigma_W} \right). \end{aligned} \quad (3)$$

Here, R represents the determinant of the symmetrical matrix \mathcal{R} of the correlation coefficients $\rho_{ij} = R_{ij}/R$ (for $i, j = U, V + 220, W$), and R_{ij} designates the cofactor of the corresponding correlation element in \mathcal{R} (e.g., Trumpler & Weaver 1953).

Figure 1 shows the kinematic distribution for the individual components, $(U, V + 220, W)$, of the space-velocity vector for the full sample of 2417 selected halo stars; the 242 objects

composing the sample of the 10% highest-velocity tail are represented with crosses.

As expected, the overall velocity distribution is relatively smooth because of the strong phase-mixing that takes place in the inner-halo region and slowly prograde (e.g., Helmi 2008).

However, as their motions (in direction and speed) are well separated from those of the other nearby subdwarfs, we intend to study the degree of clumpiness of the 10% fastest-moving objects. The case study is that of all the objects passing within a few kiloparsecs of the Sun: some are part of a diffuse local stellar halo, while some could be debris of accretion events and remnants from the outer-halo population currently in the solar neighborhood.

Before starting to look for kinematic substructures, we check for thick disk stars that could possibly contaminate our halo tracers. Here, we applied the kinematic method described in Spagna et al. (2004) and estimate the fraction of subdwarfs that is consistent with the 3D velocity distribution of the thick disk population. By assuming a velocity ellipsoid, as estimated by Pasetto et al. (2012), and a rotation velocity $V_\phi = 150 \text{ km s}^{-1}$, as measured by Spagna et al. (2010a) for metal-poor thick disk stars with $[\text{Fe}/\text{H}] \simeq -1$ dex, we found, at the 2σ confidence level (i.e., 87%), a $\sim 10\%$ maximum contamination of the thick disk in the whole sample of 2417 halo tracers. Instead, no contaminant is expected among the subsample of the 10% fastest objects.

We use the samples described above to detect and subsequently identify kinematic halo substructures in the solar neighborhood as groups of stars moving with similar velocities and directions. Detection is accomplished by performing a statistical test based on individual kinematics aimed at quantifying possible deviations from a smooth distribution of the background halo; cluster analysis in velocity space is then applied for final confirmation of the substructures.

3.2. The Two-point Correlation Function: Finding the Clumps

The amount of kinematic substructures that cosmology might leave in the volume is quantified by means of the cumulative two-point correlation function, $\xi(\nu)$, on the paired velocity difference $\nu = |\mathbf{v}_i - \mathbf{v}_j|$ that measures the excess in the number of stellar pairs moving within a given velocity difference when compared to a representative random smooth sample (see Re Fiorentin et al. 2005 for more details). Here, the random points were drawn from a multivariate distribution obtained from the observed data set by random permutations of the order of the velocity components $V + 220$ and W after fixing U ; finally, the actual random pairs were obtained after averaging over 10 independent realizations.

This function is computed over the full sample of 2417 halo stars and separately for the subsample of the 242 fastest-moving stars, corresponding to the 10% high-velocity tail.

A statistical excess of stars with small pairwise velocity differences indicates the presence of likely streamers made of objects with coherent kinematics.

Figure 2 shows, using bins of 10 km s^{-1} width,⁴ the two-point correlation function $\xi(\nu)$ for the full sample of 2417 halo stars (dots) and for the subset of the 10% fastest-moving stars (diamonds). While weak for the full sample, there is a

⁴ We fixed the bin width following the rule that the interval sampled is divided into as many bins as the square root of the sample size, in our case, $\sim 400 \text{ km s}^{-1} / \sqrt{2417} \sim 10 \text{ km s}^{-1}$.

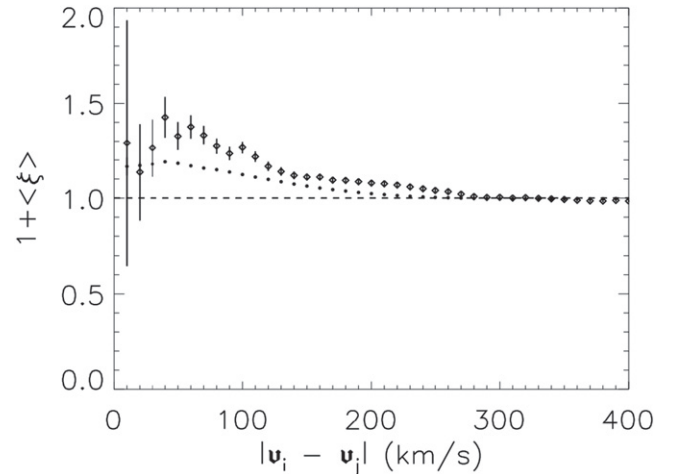


Figure 2. Cumulative velocity correlation function for the full sample of halo stars (dots) and the 10% fastest-moving subset (diamonds) shown in Figure 1. The error bars are derived from Poisson’s statistics of the counts.

statistically significant signal ($S/N > 4$) for the subset of the fastest stars that peaks at 40 km s^{-1} : the excess of pairs of stars with similar velocities is very noticeable and is a direct indication of the presence of kinematical clumps.

In the following, among the sample of the 242 fastest stars, we focus on the objects with paired velocity differences less than 40 km s^{-1} , which yield the statistically significant signal seen in Figure 2. In addition, we exclude *isolated* pairs, i.e., “groups” with only two objects. This further selection certainly reduces the number of detected members; however, it makes the following analysis more robust by decreasing the contamination of false positives. The final sample is made of 67 stars.

3.3. Clustering Analysis: Assigning Membership

In order to classify these 67 objects, we perform K -medoids clustering⁵ of the 3D velocity space that defines the number of kinematic substructures and their members. This unsupervised learning algorithm is able to group data into a pre-specified number of clusters that minimizes the rms of the distance (in velocity space) to the center of each cluster.

The original data set is initially partitioned into clusters around K data points referred to as the medoids, then an iterative scheme (PAM, for Partitioning Around Medoids) is applied to locate the medoids that achieve the lowest configuration “cost.” The algorithm employed by PAM, similar to the K -means clustering algorithm, is more robust to outliers and obtains a unique partitioning of the data without the need for explicit multiple starting points for the proposed clusters (see, e.g., Kaufmann & Rousseeuw 1990; Hastie et al. 2001).

There is no general theoretical solution for finding the optimal number of clusters for any given data set. Increasing K results in the error function values formally being much smaller, but this increases the risk of overfitting. In order to keep the final identification safe and simple, we compared the results of runs with different K classes, and the best K resulted following visual inspection of the generated distribution. The solution adopted here is with $K = 5$: for $K < 5$ the clusters

⁵ We used the implementation of the K -medoids clustering developed as part of the *R Project for Statistical Computing*: www.r-project.org.

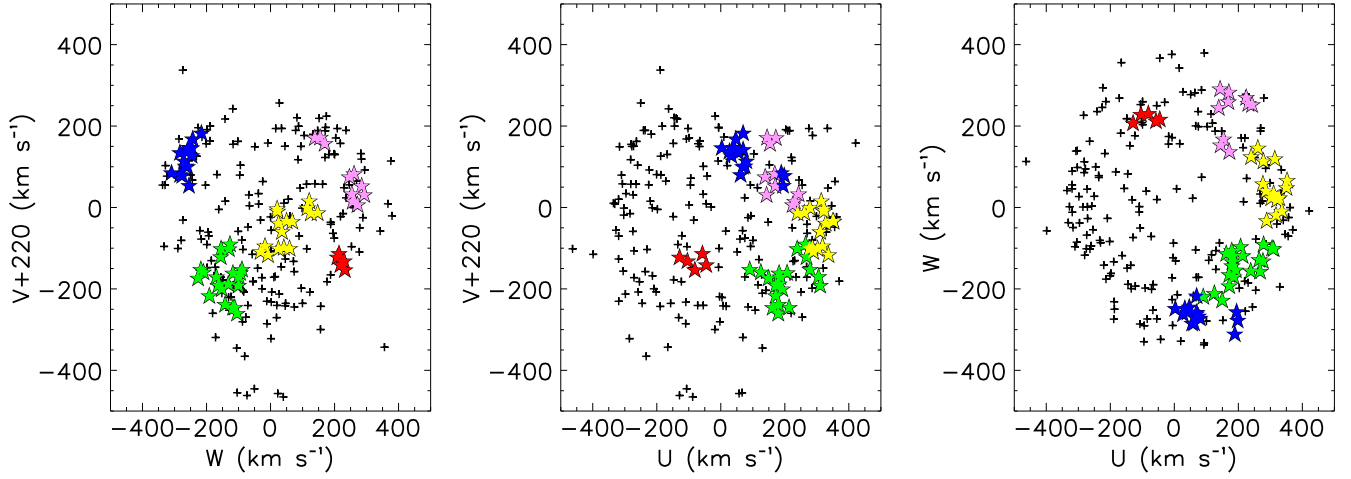


Figure 3. Distribution of the high-velocity tail from our selected sample with $[\text{Fe}/\text{H}] < -1.5$ and $|z| > 1$ kpc within 3 kpc of the Sun (see Figure 1). Shown are 242 objects, the 10% fastest-moving stars. Among them, star symbols identify the 67 sources with pairwise velocity differences below 40 km s^{-1} ; the stars belonging to isolated pairs have been excluded. Different colors are used to indicate stars associated with the five clumps recovered by the clustering analysis.

returned by the algorithm would contain a mixture of the natural underlying groups (e.g., prograde and retrograde members in the same kinematic clump); for $K > 5$ natural groups further partition into “artificial” subgroups.

The five kinematic substructures detected are visualized in Figure 3 with different colors.

The individual kinematic properties of the 67 stars belonging to the five kinematics groups are listed in Table 2.

Other methods have been utilized to isolate groups of stars in the halo, e.g., the interesting approach specifically developed for the Virgo stellar stream by Duffau et al. (2014). On the other hand, the fact that we have the complete set of 3D kinematical data and that the whole sample is confined within 3 kpc from the Sun (i.e., the distance segregation is implicitly implemented in our sample) suggests the direct use of a classical clustering algorithm like PAM as the method of choice.

3.4. Angular Momentum and Orbital Properties

The space of adiabatic invariants allows better identification of the different possible merging events that might have given rise to the observed substructures. Clumping should be even stronger since all stars originating from the same progenitor should have very similar integrals of motion, resulting in a superposition of the corresponding streams; that is, the initial clumping of satellites are present even after the system has completely phase-mixed (e.g., Helmi & de Zeeuw 2000).

In this study, we focus on the plane defined by the components of angular momentum⁶ in and out the plane of the Galaxy’s disk, i.e., L_{xy} and L_z , respectively.

Since for a local sample $(x, y, z) \sim (r_\odot, 0, 0)$, we note that $L_{xy} \sim r_\odot |v_z|$ is dominated by the velocity perpendicular to the plane and $L_z \sim r_\odot v_\phi$ measures the amount of rotation of a given stellar orbit. Essentially, stars with high/low L_{xy} are on high-/low-inclination orbits, stars with $L_z < 0$ are on retrograde orbits, and stars with $L_z > 0$ are on prograde orbits.

Figure 4 shows the distribution of the selected sample within 3 kpc of the Sun in the angular momentum diagram L_z versus

L_{xy} . As in Figure 3, the 10% fastest-moving objects are plotted as crosses, and with the star symbols we mark the group members identified in Section 3.2. Different colors indicate the stars associated with the different lumps recovered by the cluster analysis in velocity space.

The solid lines show the loci of the known kinematic structures detected by

1. Helmi et al. (1999) at $300 < L_z < 1500 \text{ kpc km s}^{-1}$ and $1400 < L_{xy} < 2500 \text{ kpc km s}^{-1}$,
2. Képley et al. (2007) at $-3000 < L_z < -1750 \text{ kpc km s}^{-1}$ and $0 < L_{xy} < 2500 \text{ kpc km s}^{-1}$,
3. Dinescu (2002) at⁷ $-600 < L_z < -200 \text{ kpc km s}^{-1}$ and $0 < L_{xy} < L_{xy}^{\text{lim}} \text{ kpc km s}^{-1}$.

The most noticeable feature in Figure 4 is certainly the kinematic group corresponding to the stream found by Helmi et al. (1999). Here, we identify 25 subdwarfs, including 4 stars already detected by Klement et al. (2009) and 21 new members. By inspection of Figure 3, we notice that the 10 members belonging to Group 1 (pink star symbols) run along near-parallel orbits and cross the Milky Way’s disk at high speed from south to north, and the 15 objects in Group 2 (blue star symbols) cross the Milky Way’s disk at similar speed and angle, but from north to south.

The three remaining lumps of fast-moving stars (red, Group 3; green, Group 4; and yellow, Group 5) appear on the retrograde side of Figure 4. The pentagonal box confined by the dashed line includes most of the members of Group 3 (5 stars), Group 4 (21 stars), and Group 5 (16 stars).

These groups, and in particular the small Group 3, do not appear to be easily associated with known streams, and in Section 5, we discuss the possibility that all these stars come from a common progenitor or from three different merging events.

Anyhow, we note that Group 4 might be the parent populations of the counter-rotating “outliers,” with $V_\phi < -250 \text{ km s}^{-1}$, found by Képley et al. (2007), while the slightly retrograde Group 5 ($V_\phi \approx -50 \text{ km s}^{-1}$) seems to be

⁶ Note that: $L_x = yv_z - zv_y$, $L_y = zv_x - xv_z$, $L_z = xv_y - yv_x$, and $L_{xy} = \sqrt{L_x^2 + L_y^2}$. Here, $v_x = -U$, $v_y = V + 220$, and $v_z = W$.

⁷ For the Dinescu (2002) region, the curve delimiting the L_{xy} upper part was derived by remapping the $L_z - L$ region shown in Figure 4 of that paper; therefore, $671 < L_{xy}^{\text{lim}} < 922$.

Table 2
Main Individual Characteristics of the 67 Fastest-moving Stars Found Members of Five Different Kinematics Groups

Group	ID	U (km s ⁻¹)	$V + 220$ (km s ⁻¹)	W (km s ⁻¹)	L_{xy} (kpc km s ⁻¹)	L_z (kpc km s ⁻¹)	[Fe/H] (dex)
1 ^a /pink	52209-0694-596	143 ± 14	33 ± 12	293 ± 6	2289	389	-2.01
	52721-1050-418	145 ± 7	173 ± 6	155 ± 4	1390	1473	-2.02
	53315-1907-393	170 ± 31	54 ± 31	285 ± 16	2232	614	-1.75
	53349-2066-511	154 ± 23	158 ± 28	169 ± 27	1459	1678	-1.85
	54175-2472-370	139 ± 13	76 ± 16	246 ± 4	2336	634	-1.75
	54574-2904-114	243 ± 9	35 ± 9	254 ± 3	2301	316	-1.94
	54577-2906-088	225 ± 12	8 ± 12	272 ± 5	2532	198	-2.16
	54621-2191-177	231 ± 11	16 ± 11	257 ± 10	2045	405	-1.81
	54624-2189-236	169 ± 17	84 ± 26	261 ± 23	1820	590	-1.73
	54629-2902-237	172 ± 7	172 ± 9	138 ± 6	1216	1203	-2.64
2 ^a /blue	52316-0559-336	189 ± 3	87 ± 11	-310 ± 5	2545	853	-2.52
	53084-1368-399	195 ± 5	55 ± 6	-255 ± 4	1906	517	-2.16
	53242-1896-109 ^b	41 ± 14	149 ± 11	-256 ± 7	2220	1299	-1.66
	53262-1900-359	62 ± 19	82 ± 21	-283 ± 17	2215	706	-2.09
	53293-1906-633 ^b	27 ± 6	139 ± 7	-261 ± 5	2281	1210	-1.91
	53467-2110-134	69 ± 10	102 ± 11	-260 ± 3	1921	815	-1.55
	53712-2314-639	75 ± 5	103 ± 6	-265 ± 5	2387	936	-2.57
	53726-2306-188 ^b	55 ± 9	136 ± 10	-283 ± 7	2555	1218	-1.74
	53907-2209-540 ^b	70 ± 13	144 ± 12	-256 ± 13	1663	1011	-2.30
	54178-2452-540	70 ± 6	184 ± 7	-216 ± 3	1735	1556	-1.51
	54380-2323-448	47 ± 15	170 ± 13	-243 ± 13	1858	1324	-2.12
	54479-2867-531	33 ± 14	129 ± 11	-246 ± 12	2153	1097	-1.64
	54530-2889-458	3 ± 4	148 ± 9	-247 ± 4	2238	1342	-1.56
	54554-2918-615	198 ± 15	80 ± 15	-276 ± 3	2004	604	-1.98
54580-2905-169	80 ± 10	115 ± 11	-271 ± 4	1923	873	-1.71	
3 ^c /red	54179-2567-458	-57 ± 12	-112 ± 16	214 ± 8	1922	-1076	-1.64
	54463-2856-571	-129 ± 9	-121 ± 22	209 ± 6	1617	-1089	-2.09
	54551-2394-228	-104 ± 10	-130 ± 14	230 ± 8	1924	-1234	-1.72
	54562-2920-596	-81 ± 19	-152 ± 19	232 ± 10	1521	-1032	-2.36
	54569-2900-046	-46 ± 7	-139 ± 8	218 ± 3	1712	-1139	-1.68
	52059-0597-072	125 ± 4	-157 ± 10	-210 ± 6	1672	-1280	-2.09
4 ^c /green	52338-0788-070	180 ± 9	-237 ± 11	-142 ± 9	921	-1767	-2.07
	52942-1509-488	179 ± 9	-259 ± 22	-105 ± 8	1137	-2235	-1.64
	53710-2310-141	207 ± 39	-159 ± 16	-95 ± 20	1195	-877	-1.60
	53762-2381-588	213 ± 16	-244 ± 29	-117 ± 14	916	-2517	-1.85
	53800-2383-625	172 ± 7	-190 ± 14	-164 ± 8	1275	-1652	-1.69
	53823-2240-213	310 ± 22	-190 ± 26	-100 ± 4	557	-1513	-1.70
	53874-2173-414	279 ± 16	-151 ± 18	-89 ± 12	199	-688	-1.57
	54154-2701-341	171 ± 10	-216 ± 16	-191 ± 21	1826	-2236	-1.74
	54169-2413-090	149 ± 12	-172 ± 12	-226 ± 7	1711	-1626	-1.77
	54234-2663-321	90 ± 11	-151 ± 13	-218 ± 3	1581	-1187	-2.16
	54539-2894-314	162 ± 3	-244 ± 12	-112 ± 5	793	-2008	-2.12
	54539-2894-632	305 ± 6	-168 ± 6	-99 ± 3	478	-1299	-1.59
	54544-2459-072	239 ± 7	-100 ± 8	-154 ± 7	802	-532	-1.82
	54557-2177-009	277 ± 16	-100 ± 18	-130 ± 10	507	-454	-2.73
	54568-2899-316	182 ± 17	-160 ± 25	-117 ± 4	665	-1294	-1.92
	54595-2932-091	268 ± 17	-120 ± 15	-156 ± 7	737	-704	-1.63
	54597-2561-326	265 ± 15	-89 ± 3	-127 ± 4	750	-289	-1.96
54616-2460-420	186 ± 8	-169 ± 9	-169 ± 9	1180	-1246	-1.93	
54616-2460-616	192 ± 16	-199 ± 15	-152 ± 16	977	-1450	-1.98	
54631-2911-151	182 ± 11	-187 ± 11	-132 ± 8	710	-1212	-1.96	
5 ^c /yellow	53035-1433-600	322 ± 10	-8 ± 13	22 ± 6	1004	-56	-1.58
	53240-1894-079	277 ± 22	-99 ± 18	59 ± 18	120	-273	-2.10
	53315-1907-353	352 ± 35	-33 ± 35	68 ± 18	258	-32	-1.50
	53770-2387-010	322 ± 6	-2 ± 12	21 ± 4	559	-66	-1.67
	53848-2437-060	314 ± 13	17 ± 22	121 ± 13	1787	-228	-2.18
	53876-2134-516	318 ± 13	-94 ± 13	-17 ± 5	528	-518	-1.52
	53918-2539-196	240 ± 10	-13 ± 8	126 ± 8	1356	121	-1.93
	54082-2325-126	278 ± 23	0 ± 16	115 ± 15	468	420	-1.61
	54156-2393-459	336 ± 11	-115 ± 9	-8 ± 5	527	-1231	-1.74
	54243-2176-476	350 ± 6	-32 ± 4	50 ± 4	795	131	-1.73
	54271-2449-590	261 ± 11	-12 ± 9	147 ± 7	1686	321	-2.21
	54368-2804-351	302 ± 15	-100 ± 19	24 ± 19	332	-523	-1.67

Table 2
(Continued)

Group	ID	U (km s ⁻¹)	$V + 220$ (km s ⁻¹)	W (km s ⁻¹)	L_{xy} (kpc km s ⁻¹)	L_z (kpc km s ⁻¹)	[Fe/H] (dex)
	54536-2871-426	286 ± 21	-97 ± 40	42 ± 11	1155	-888	-1.93
	54594-2965-227	288 ± 14	-107 ± 16	-31 ± 6	387	-974	-1.64
	54594-2965-272	328 ± 14	-37 ± 12	25 ± 5	782	-448	-1.54
	54616-2929-342	310 ± 7	-58 ± 8	36 ± 2	625	-403	-1.60

Notes. Main individual characteristics of the 67 selected fastest-moving stars with paired velocity differences less than 40 km s⁻¹ and belonging to 5 different kinematics groups. These are 25 subdwarfs (21 new) on 2 streamers (Group 1 and Group 2), both members of the Helmi et al. (1999) stream, originally made of red giants and RR Lyrae. The remaining 42 are subdwarf members of 3 newly discovered kinematic groups (Group 3, 4, and 5); see the text for their dynamical interpretation.

^a Subdwarf members associated with the Helmi et al. (1999) stream.

^b Subdwarf members classified by Klement et al. (2009).

^c Subdwarf members of the newly discovered kinematic groups.

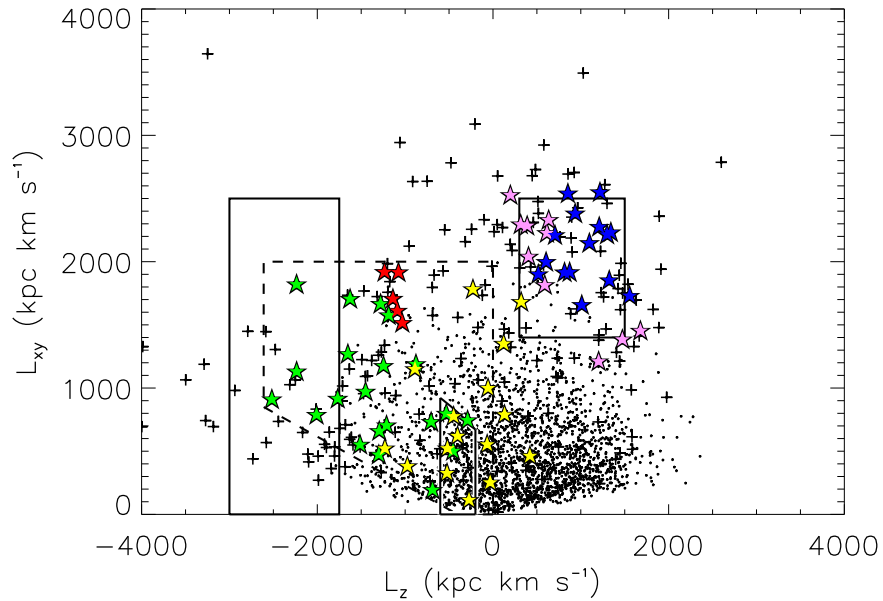


Figure 4. Distribution of the selected sample of 2417 FGK subdwarfs within 3 kpc of the Sun in the space of adiabatic invariants. Cross symbols indicate the 10% fastest-moving objects. Among them, star symbols identify the 67 sources with paired velocity differences below 40 km s⁻¹. As in Figure 3, different colors are used to indicate stars associated with the five clumps recovered by the clustering analysis in velocity space. At $L_z > 0$, the solid box shows the locus of the halo stream discovered by Helmi et al. (1999); the kinematic substructures, pink and blue stars (i.e., Groups 1 and 2 in Table 2), on prograde orbits indeed cover the same region. At $L_z < 0$, the solid box at $L_z \sim -2375$ shows the locus of the substructure detected by Kepley et al. (2007) as retrograde outliers, while the solid contour at $L_z \sim -400$ identifies the ω Cen substructures remapped from the $L_z - L$ region in Dinescu (2002). The area within the dashed line includes the kinematic Groups 3, 4, and 5 of Table 2, represented by the red, green, and yellow stars, respectively.

related to the kinematic structure found by Dinescu (2002) and confirmed by both Meza et al. (2005) and Majewski et al. (2012). These authors have also discussed the possibility that such a stream is formed by the tidal debris of ω Cen in the solar neighborhood, even though Navarrete et al. (2015) have recently ruled out this hypothesis after detailed analysis of the chemical abundance of this group with respect to the well-known peculiar properties of ω Cen.

4. SIMULATIONS

We explore a simulated inner halo based on a set of *four* high-resolution numerical N -body simulations of minor mergers. We analyze the kinematics and orbital properties of these simulations in order to investigate and characterize detectable signatures.

It is useful to point out that these simulations are not an attempt to “fit” the observations, but they represent four merging events that we assume as representative, in terms of inclination and rotation, of the initial orbits of the satellites. In particular, these choices allow us to analyze the two cases suffering maximum and minimum dynamical friction.

4.1. N -body Simulations

We use a set of high-resolution numerical N -body simulations that simulate minor mergers of prograde and retrograde orbiting satellite halos within a dark matter main halo (Murante et al. 2010). The main DM halo, which contains a stellar, rotating exponential disk, has a Navarro–Frenk–White radial density profile (Navarro et al. 1997), with a mass ($M_{200} = 10^{12} M_{\odot}$), radius ($R_{200} = 165$ kpc), and concentration ($C_{200} = 7.5$), appropriate for a Milky Way–like DM halo at redshift $z = 0$;

Table 3

Physical Properties of the Halos: Main System and Orbiting Satellite

System	M_{DM}	M_*	N_{DM}	N_*	r_0	r_{disk}
Main	10^{12}	5.7×10^{10}	10^6	10^6	4	20
Satellite	2.4×10^9	2.4×10^{10}	1.1×10^5	10^5	0.709	...

Notes. Column 1: main galaxy/impacting system. Column 2: DM mass, in M_\odot . Column 3: stellar mass for disk/bulge in the main/satellite, in M_\odot . Column 4: DM particles. Column 5: stellar particles for disk/bulge in main/satellite. Column 6: disk scale radius for the main halo, in kpc; Hernquist scale radius for the satellite, in kpc. Column 7: disk truncation radius, in kpc.

the spin parameter is set⁸ to $\lambda = 1$. The satellite is represented by a secondary DM halo containing a stellar bulge and a Hernquist radial density profile (Hernquist 1993); the spin parameter is set to $\lambda = 0$. The mass ratio, $M_{\text{primary}}/M_{\text{satellite}} \sim 40$, is similar to the estimated mass ratio of the Milky Way relative to the Large Magellanic Cloud. The main physical parameters of our simulated mergers are listed in Table 3.

We consider prograde mergers, in which the satellite co-rotates with the spin of the disk, as well as retrograde mergers, with a counter-rotating satellite. We analyze two orbits: a low-inclination orbit with a 10° tilt with respect to the disk plane and a high-inclination orbit with a 60° tilt.

Initially, the particles of the small system (satellite galaxy) orbiting around the (otherwise static) disk galaxy are all strongly concentrated in space and share essentially the same motion. The initial conditions (inclination, position, and velocity) of the main system and the four impacting satellites, cosmologically motivated (Read et al. 2008; Villalobos & Helmi 2008), are summarized in Table 4.

From the grid of simulations by (Read et al. 2008), we chose four impactors, all of which have the mass of the Large Magellanic Cloud. Larger masses would affect the stability of the stellar disk, and this is not consistent with a Milky Way-like galaxy. Conversely, smaller masses would produce minor signatures in our local halo sample.

The four simulations are compiled using the public parallel Treecode GADGET2 (Springel 2005) on the cluster matrix at the CASPUR (*Consorzio Interuniversitario per le Applicazioni del Supercalcolo*) consortium, Rome. All systems were left to evolve for 4.63 Gyr (about 16 dynamical timescales of the main halo). After this time, the four satellites have completed their merging with the primary halo. The final (x, z) distribution of the inner satellite star particles and host disk, in both the retrograde and prograde cases, as well as for the high and low inclinations, is shown in Figure 5.

4.2. Dynamical Friction and Tidal Stripping

Any satellite can in principal be slowed by dynamical friction exerted on it by disk and halo particles. It is known that an object, such as a satellite, of mass M , moving through a homogeneous background of individually much lighter particles with an isotropic velocity distribution suffers a drag force

(Chandrasekar 1943):

$$F_d = -\frac{4\pi G^2 M^2 \rho_f \langle v_s \rangle \ln \Lambda}{v_s^2},$$

where v_s is the speed of the satellite with respect to the mean velocity of the field, $\rho_f \langle v_s \rangle$ is the total density of the field particles with speeds less than v_s , and $\ln \Lambda$ is the Coulomb logarithm (Binney & Tremaine 1987).

We expect that the higher the v_s , the weaker is the dynamical friction force. Retrograde satellites are expected to suffer weaker dynamical friction with respect to prograde ones since in the first case the velocity of the satellite is opposite to that of the disk. As a consequence, prograde orbits decay faster. This effect is even more evident for low-inclination orbits.

Another important effect that occurs during mergers is the tidal disruption of satellites. While tidal disruption is most important near the center of the main halo, where the gravitational potential is changing more rapidly, dynamical friction is exerted both by the main halo DM particles and by the disk star particles.

4.3. Debris in the Local Halo

We analyze the observational signature left by the satellite stars after selecting particles in a sphere of 3 kpc radius centered at the Sun ($x = 8$ kpc from the Galaxy center) and with $|z| > 1$ kpc. This last constraint is introduced so that the simulated and observed samples can be compared within a similar volume of the inner halo.

Figure 6 shows the kinematic distribution (velocity projections) of our simulated inner halo. The different colors indicate the association of the 3902 debris stars with different progenitors: the low-/high-inclination retrograde satellites (761/616 green/red dots) and the high-/low-inclination prograde satellites (966/1559 blue/yellow dots).

The angular momentum distribution of the satellite debris is shown in Figure 7. Despite the chaotic build-up of the parent halo, it appears that objects from accreted satellites remain confined in limited portions of the (L_z, L_{xy}) plane.

The satellite on a low-inclination prograde orbit (yellow particles), which suffers more from dynamical friction, quickly loses its orbital energy and proceeds to the inner regions of the main halo (Byrd et al. 1986; Murante et al. 2010). For this reason, fewer particles are left in the outer halo; see the top right panel of Figure 5.

It is worth noting that the high-inclination prograde satellite suffers the effect of dynamical friction as well, as a result of its co-rotation with the disk. This effect acts in producing a consistent mass of debris in the solar region with L_{xy} ranging between 500 and 1500 kpc km s⁻¹ (blue points in Figure 7).

On the other hand, retrograde satellites experience weaker dynamical friction and leave more particles in the outer-halo region since their orbits have a longer decay time and longer periods. Thus, tidal stripping (see, e.g., Colpi et al. 1999) can act longer and more efficiently when the satellite is still orbiting at high velocity, and we see that a better populated high-velocity tail results (compare Figure 7 to Figure 10).

The impact of dynamical friction on the two configurations considered for the retrograde satellites indicates that the high-inclination case is the one less affected by this force, which again results in efficient stripping when the satellite has high orbital velocity. Therefore, such stripping takes place over a

⁸ The cases $\lambda = 0$ and $\lambda = 1$ were both studied at lower resolution and the results were compared; the differences are such that they have no bearing on the results presented in this paper.

Table 4
Initial Conditions of the Main System and the Four Impacting Satellites

System	Inclination	Rotation	x (kpc)	y (kpc)	z (kpc)	v_x (km s^{-1})	v_y (km s^{-1})	v_z (km s^{-1})	v (km s^{-1})
Main	0°	...	0.00	0.00	0.00	0.00	0.00	0.00	0.00
Satellite 1	10°	retrograde	80.00	0.27	15.20	6.30	-62.50	0.35	62.82
Satellite 2	10°	prograde	80.00	0.27	15.20	6.30	62.50	0.35	62.82
Satellite 3	60°	retrograde	15.00	0.12	26.00	1.20	80.10	2.00	80.13
Satellite 4	60°	prograde	15.00	0.12	26.00	1.20	-80.10	2.00	80.13

Note. Inclination and rotation of the orbit, position, and velocity components and total velocity.

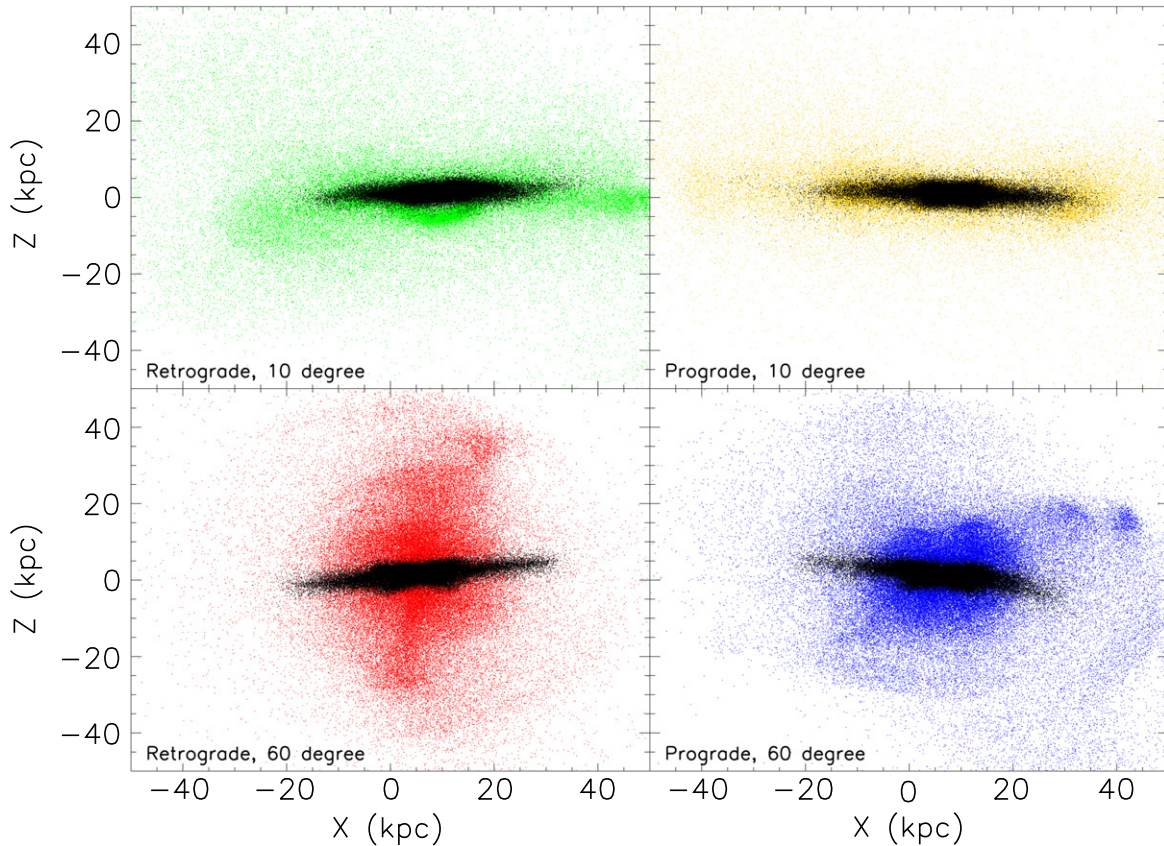


Figure 5. Final configurations in the (x, z) plane of four minor merger events: depicted are the morphologies of the stellar distribution, i.e., the host disk (black) and the satellite bulge (color), at the final time $T = 4.63$ Gyr of the simulations. Shown are the cases of low-inclination (10° tilt) retrograde (top left)/prograde (top right) orbit and of high-inclination (60° tilt) retrograde (bottom left)/prograde (bottom right) orbit. The panels only display a randomly selected 10% subset of the total particles utilized.

large spatial region, and for the conservation of 6D phase-space density, by virtue of Liouville’s Theorem, we expect a small variance in velocity space and in the plane of angular momenta. This is indeed observed for the red particles with respect to the green ones in Figures 6 and 7.

Finally, the effect of both gravitational feedback and dynamical friction on the satellites, which lead to a loss of stars at different passages with different energies, is clearly evident for the case of low-inclination prograde orbit in Figure 7 at around $L_{xy} = 400 \text{ kpc km s}^{-1}$ and $L_z = 1750 \text{ kpc km s}^{-1}$.

5. “OBSERVED” SIMULATIONS

Here, we investigate the effects of observational errors on our simulated data and show how more accurate kinematic data

to be provided by future surveys can improve detection and characterization of halo streams. Moreover, we compare *actual* observations with the distributions of debris resulting from the four simulated satellites presented in the previous section and discuss the orbital properties of the parent dwarf galaxies possibly responsible for accreting on the Milky Way halo.

5.1. Observational Errors

We perturb the original simulations by convolving the “true” data with two cases of error distributions. First, we adopt the accuracy of our SGKS catalog as representative of the quality of current wide-field surveys. Then, we assume the mean accuracy expected from the forthcoming *Gaia* catalog combined with complementary deep spectroscopic data from ongoing and future surveys such as GES (Gilmore et al. 2012).

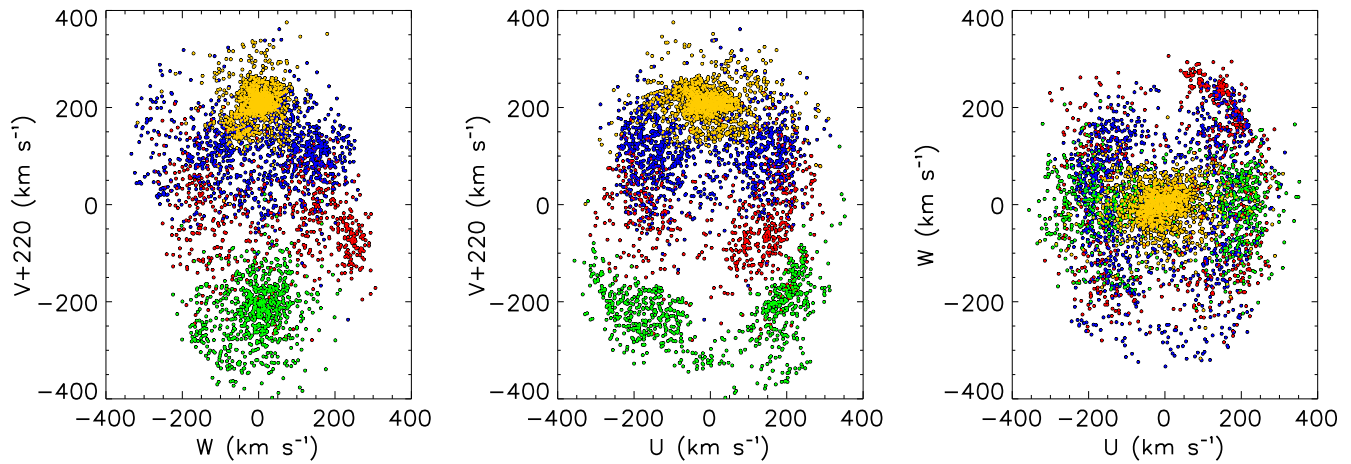


Figure 6. Kinematical (velocity space) distribution of the accreted component of the simulated Milky Way inner halo, i.e., 3902 particles in a spherical volume of radius 3 kpc centered on the “Sun” with $|z| > 1$ kpc. Different colors indicate particles associated with different satellites: 60° retrograde/prograde (red/blue), 10° retrograde/prograde (green/yellow) colliding satellites.

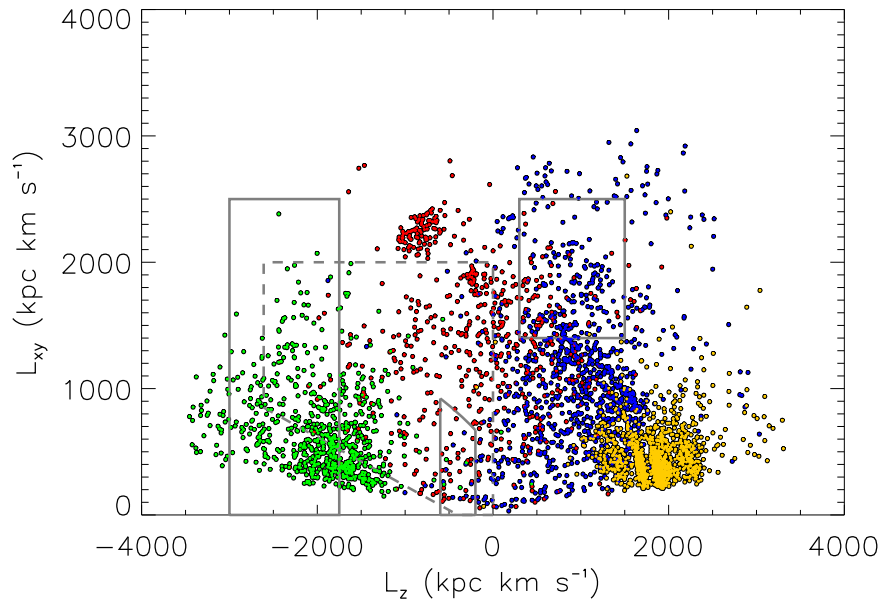


Figure 7. Angular momentum distribution of the simulated Milky Way halo within 3 kpc of the “Sun.” As in Figure 6, shown are the 3902 particles accreted from four dwarf galaxies: 60° retrograde/prograde (red/blue), 10° retrograde/prograde (green/yellow) satellites after interaction with the simulated Milky Way. All of the marked regions have the same meaning as in Figure 4.

The true positions and velocities of each particle are first transformed into their astronomical observables (α , δ , $m - M$, or π and μ_α , μ_δ , V_r); then, the expected observational errors are added to distance modulus (or directly to parallax, in the case of the *Gaia*-like simulation), radial velocity, and proper motion, according to Table 5.

The precision in distance is taken to $\sigma_{m-M} = 0.4$ mag (i.e., $\sigma_d/d \simeq 20\%$) for the photometric distances estimated from the SGKS catalog and to $\sigma_\pi = 20 \mu\text{as}$ for the final precision on trigonometric parallaxes measured by *Gaia*. In proper motion, the precision is assumed to be 2 mas yr^{-1} for ground-based observations and $20 \mu\text{as yr}^{-1}$ for *Gaia*. The precision in the radial velocity is taken to be 10 km s^{-1} for the SDSS measurements and 1 km s^{-1} for the GES spectroscopic survey. These quantities are finally transformed back to observed positions vectors and space velocities.

Table 5
Estimated/Expected Errors for the SGKS and *Gaia* Catalogs

Catalog	Distance	Proper Motion	Radial Velocity
SGKS	$\sigma_{m-M} = 0.4$ mag	2000	10
<i>Gaia</i> /GES	$\sigma_\pi = 20 \mu\text{as}$	20	1

Note. Estimated errors (precision) in parallax (σ_π , in μas), distance modulus (σ_{m-M} , in mag), proper motion (σ_μ , in $\mu\text{as yr}^{-1}$), and radial velocity (σ_{V_r} , in km s^{-1}) for the SGKS and *Gaia* catalogs.

5.2. The Inner Halo Model

We explore a simulated inner halo based on the superposition of the four simulations of minor mergers and a smooth local component with the same kinematic properties of the observed sample (Table 1).

Table 6
Composition of the 10% High-velocity Tail of the Simulated Milky Way Halo

Catalog	Halo+Debris	Debris	Satellite 1	Satellite 2	Satellite 3	Satellite 4
“True” Simulation	2874	1103 (0.38%)	262	201	601	39
“Observed” SGKS	2874	835 (0.29%)	233	170	406	26
“Observed” <i>Gaia</i> /GES	2874	1061 (0.37%)	263	191	570	37

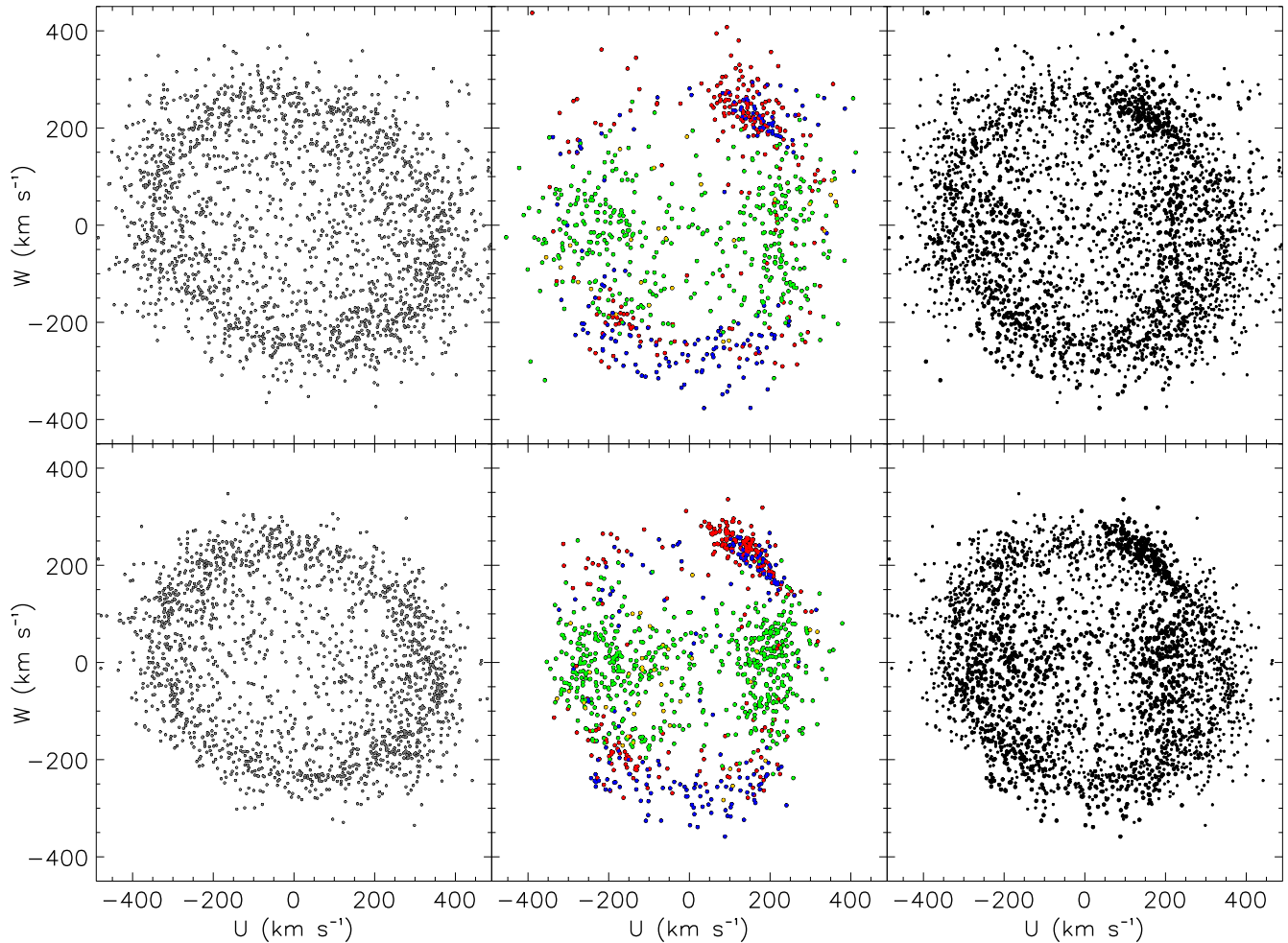


Figure 8. (U, W) velocity distribution of the 10% high-velocity tail of the simulated sample is shown in the right panels. The sample is limited to a spherical volume of radius 3 kpc located on the plane of the simulated Milky Way 8 kpc away from its center and with $|z| > 1$ kpc. Of the 2874 particles in this sample, some are remnants of the four satellites accreted after 5 Gyr (middle panels), the remaining constitute the “background” of smooth inner-halo stars (left panels). Different colors represent different progenitors as in Figure 5. Finally, the top panels were generated via convolution with current, i.e., SGKS, ground-based errors, while the bottom figures depict the results after convolution with the expected *Gaia*-like errors.

Consistent with the findings of Helmi et al. (1999) and Kepley et al. (2007), we assumed a debris total fraction of 10% within 3 kpc from the Sun.

In the “true” (simulated) catalog, of the 28,738 particles with $|z| > 1$ kpc, 24,836 are part of the local mock halo, while the remaining 3902 are debris from the satellites shown in Figures 6 and 7.

In the following discussion, we focus on the particles of the accreted component that belong to the 10% high-velocity tail. Table 6 reports the number of particles belonging to each satellite for the pure simulation and the other two cases accounting for observational errors.

Figure 8 shows the region of the (U, W) plane occupied by the 10% high-velocity tail of the resulting simulated Milky Way inner halo (right panels) as a superposition of the accreted component (middle panels) and the smooth spheroid (left panels). The synthetic “observed” catalog shown in the top panels represents the current picture, according to the SGKS-error model. The bottom panels show the distribution of the high-velocity particles as promised by *Gaia*.

The upper panels indicate that distinguishing in velocity space the satellites that gave rise to each of the different moving groups with the extant data is a non-trivial task. On the other hand, as inspection of the lower panels reveals,

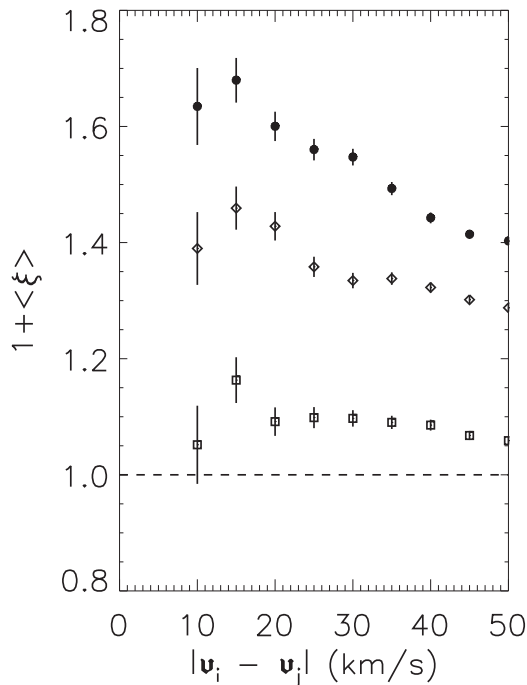


Figure 9. Cumulative velocity correlation functions for the 2874 halo particles shown in Figure 8. The filled dots trace the correlation function of the pure simulation, while squares and diamonds depict the correlation after convolution with current (i.e., SGKS) or *Gaia*/GES-like errors, respectively. Error bars are derived from Poisson’s statistics of the counts.

much of the substructures shown in the middle panels becomes visible again thanks to the superior precision that *Gaia* will achieve.

5.3. Substructures in the Correlation Function

In order to quantify the amount of kinematic substructures present among the 2874 fastest-moving particles, we compute the cumulative velocity correlation function described in Section 3.2. The analysis is performed over three synthetic catalogs: the “true” simulation and two lists derived from the true values after perturbing them with either SGKS-like errors or the errors expected for the *Gaia*/GES surveys.

Figure 9 shows, using bins of width 5 km s^{-1} up to kinematical separations of 50 km s^{-1} , the results for the two-point correlation function $\xi(\mathbf{v})$ for the “true” case (dots), the SGKS-like (squares) catalog, and *Gaia*/GES-like (diamonds) catalog. The clear signal in the first bins, peaking at $\Delta v \sim 15 \text{ km s}^{-1}$, evidences an excess of particles moving with similar velocities with respect to what was expected from a fully random sample. In the case of the pure simulation, the two-point velocity correlation function attains a maximum signature of $\langle \xi \rangle = 0.68 \pm 0.04$. For the SGKS-like catalog, the maximum signal has an $\sim 80\%$ drop to an “observed” value of $\langle \xi \rangle = 0.16 \pm 0.04$.

The recovery of the intrinsic correlation signal is truly remarkable when looking at the correlation function for the *Gaia*-like case: in fact, we measure $\langle \xi \rangle = 0.46 \pm 0.04$, corresponding to 68% of the original signal. Figure 8 provides a nice “visual” confirmation of the recovery in substructure visibility.

6. ON THE NATURE OF THE HIGH-VELOCITY DEBRIS

As the space of adiabatic invariants is important to gain more insight into the properties of the kinematic substructures detected (Section 3.4), we compare the (L_z, L_{xy}) distributions of the observed groups with the results of the simulations, taking into account the effect of the observational errors. This is shown in Figure 10, where the top panel corresponds to the SGKS-error simulation, while the bottom panel reproduces what will hopefully be seen with the final *Gaia* catalog.

The black star symbols in the upper panel of Figure 10 represent the 67 high-velocity objects we found from our statistical analysis in the same volume and shown in Figure 4 as colored stars. With current data, different satellites mix over some regions so that a discrete classification is not always straightforward. The bottom panel of Figure 10 clearly shows that this situation is highly improved with *Gaia*-like data.

We see that our Groups 1 and 2, corresponding to the stream of Helmi et al. (1999), are consistently associated with the high-inclination prograde satellite (blue dots). Because of dynamical friction (cf. Section 4.3), this satellite includes a low L_{xy} component shown in the full sample (Figure 7) that is not part of the high-velocity tail (Figure 10). Thus, these simulated “observations” suggest the possible presence in the Helmi et al. (1999) stream of debris with lower L_{xy} yet to be discovered.

Of particular interest is the case of the retrograde kinematic groups. In fact, neither the high-inclination simulated satellite nor the one at low inclination appear to fairly match the observed Groups 3, 4, and 5, i.e., the black stars with $L_z \lesssim 0$ in Figure 10.

Actually, these three groups appear to occupy an *intermediate* region between the debris of the two simulated retrograde satellites. Furthermore, in Section 3.4, we note that the observed Groups 3, 4, and 5 do not match well the streams detected by Dinescu (2002) and Képley et al. (2007). For this reason, we suggest that these three groups may represent the debris of a unique progenitor accreted along an initial retrograde orbit having an intermediate inclination in the range comprised between 10° and 60° . Alternatively, these groups could belong up to three different impacting satellites on retrograde orbits with inclinations in that same range.

The results presented in this section show that the methodology proposed is certainly capable of detecting fossil signatures as kinematic substructures among high-velocity stars. From the data at our disposal, there is clear indication that more debris are found from dwarf galaxies on high-inclination prograde and retrograde orbits, as well as on low-inclination retrograde ones. We have not identified any debris coming from low-inclination prograde satellites; however, this might be a limitation intrinsic to the methodology of looking at structures in the space motions of very high-velocity stars. Future work will have to investigate these issues.

7. CONCLUSIONS

We have explored the solar neighborhood of the Milky Way through the use of spectrophotometric data from the Sloan Digital Sky Survey and high-quality proper motions derived from multi-epoch positions extracted from the Guide Star Catalog II database. A sample with accurate distances, space velocities, and metallicities is selected as a tracer of the inner-halo population resulting in 2417 subdwarfs with $[\text{Fe}/\text{H}] < -1.5$ and $|z| > 1 \text{ kpc}$ within 3 kpc of the Sun. This

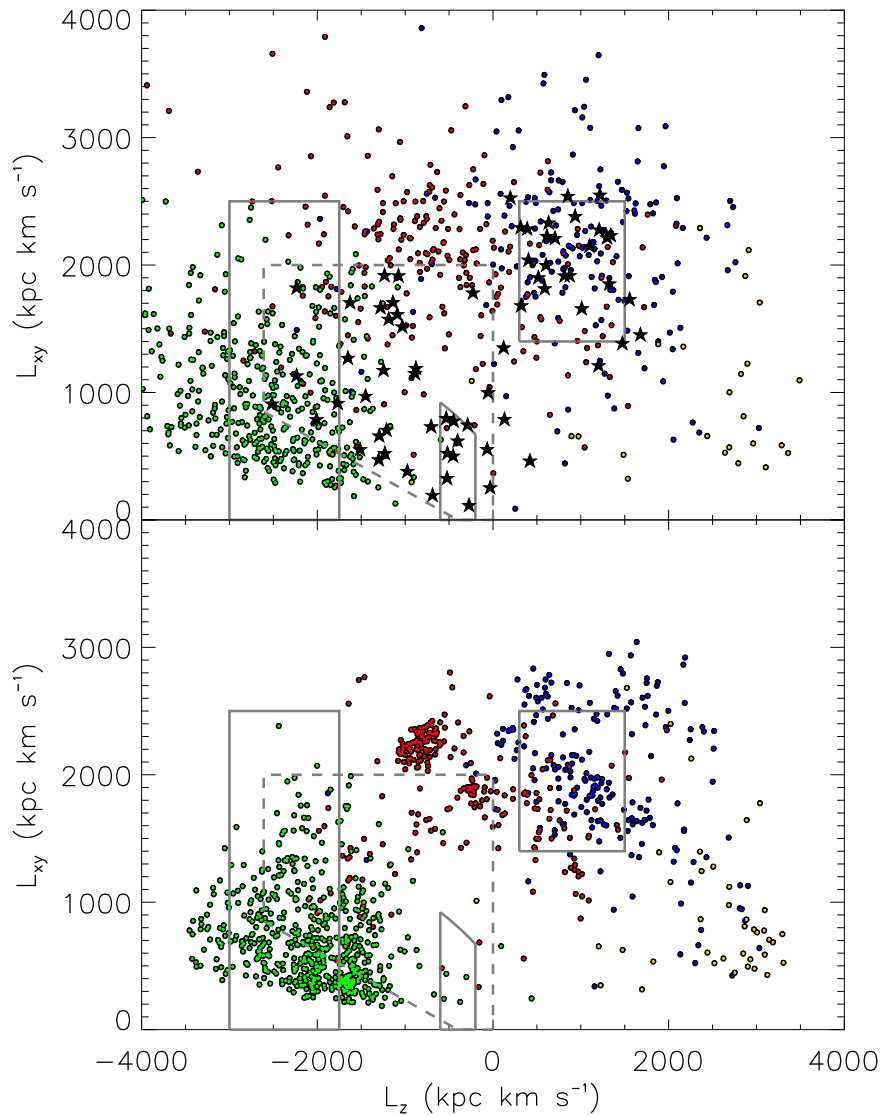


Figure 10. 10% high-velocity tail component belonging solely to the four satellites, convolved with current ground-based errors (top, 835 particles) and with the expected *Gaia* errors (bottom, 1061 particles). Black star symbols are the 67 fast-moving debris stars uncovered from the analysis of the SGKS sample. Solid and dashed contours have the same meaning as in Figures 4 and 7.

set is then analyzed to identify and characterize kinematic streams possibly arising from merging events.

We have found statistical evidence of substructures in the space motions of the 10% fastest stars, confirming the existence of five moving groups.

In angular momenta space, the two prograde groups we have identified (Groups 1 and 2 in Table 2) appear confined in the region encompassing the stream first identified by Helmi et al. (1999) among red giants and RR Lyrae within 1 kpc of the Sun. Our analysis found 25 additional subdwarf members belonging to that same stream: four are in common with those found by Klement et al. (2009), while the other 21 are newly discovered members.

Of the remaining groups, the most counter-rotating one (Group 4) partially overlaps with the region of “retrograde outliers” found by Kepley et al. (2007), while a dozen stars belonging to Group 4 and Group 5 fall in the region of the mildly retrograde stream detected by Dinescu (2002).

Comparison to our high-resolution N -body simulations confirms that the two groups associated with the Helmi stream

are likely fossil remnants of a dwarf galaxy that co-rotates with the disk of the Galaxy and moves on a high-inclination orbit.

As for the three retrograde groups (3, 4, and 5 in Table 2), they may be debris of a unique progenitor accreted along an initial retrograde orbit having an intermediate inclination in the range $10^\circ \div 60^\circ$. However, we cannot exclude that these groups belong to different impacting satellites on retrograde orbits with inclinations within that same range. A more detailed analysis of the chemical abundances of the three detected groups, as well as more quantitative comparisons to extended simulations, are necessary to resolve this issue.

In any event, the fastest objects appear with positive and negative L_z values (i.e., prograde and retrograde motions, respectively) in the angular momentum (L_z, L_{xy}) regions for high-inclination orbits ($L_{xy} \gtrsim 1500$ kpc km s $^{-1}$). On the other hand, for low-inclination orbits, both observations and simulations show that the fastest objects appear only on *retrograde* orbits (e.g., Figure 10, top panel). This asymmetric distribution is suggestive of the role played by dynamical friction during accretion.

In anticipation of the much improved data expected over the coming years, in particular from the *Gaia* catalog and new ground-based spectroscopic surveys, we also investigated the impact of observational errors in our dynamical simulations. The analysis indicates that (see the relevant panels of Figures 8 and 10) *Gaia* will greatly influence these studies: velocity and angular momentum distribution will be almost completely dominated by the physics we are trying to recover, i.e., the dynamical history of the merging events.

At that point, full grids (in, e.g., inclination and amount of rotation) of prograde and retrograde high-resolution satellite simulations will be required to precisely characterize the debris detected. Then, we will be able to number the merging events for direct comparison with the predictions of the (Λ) CDM theory and its associated merging paradigm.

In conclusion, the results shown might lead us to claim that the inner halo might have “seen” only two events; however, the large uncertainties in the extant data, mostly observational, do not exclude the possibility that the events might be as many as four, and perhaps more, given the intrinsic difficulty of our technique in dealing with low-inclination prograde mergers.

We are grateful to the referee for comments that helped us improve the original manuscript. This work has been partially funded by ASI, under contract to INAF I/058/10/0 “*Gaia* Mission—The Italian Participation to DPAC,” and by MIUR, through PRIN 2012 grant No. 1.05.01.97.02 “Chemical and dynamical evolution of our Galaxy and of the galaxies of the Local Group.” M.G.L. acknowledges support from the Chinese Academy of Sciences through 2015 CAS President’s International Fellowship Initiative (PIFI) for Visiting Scientists.

REFERENCES

- Abadi, M. G., Navarro, J. F., & Steinmetz, M. 2006, *MNRAS*, **365**, 747
- Abazajian, K. N., Adelman-McCarthy, J. K., Agüeros, M. A., et al. 2010, *ApJS*, **182**, 543
- Allende Prieto, C., Sivarani, T., Beers, T. C., et al. 2008, *AJ*, **136**, 2070
- Binney, J., & Merrifield, M. 1998, *Galactic Astronomy* (Princeton, NJ: Princeton Univ. Press)
- Binney, J., & Tremaine, S. 1987, *Galactic Dynamics* (Princeton, NJ: Princeton Univ. Press)
- Bond, N. A., Ivezić, Ž., Sesar, B., et al. 2010, *ApJ*, **716**, 1
- Bullock, J. S., & Johnston, K. V. 2005, *ApJ*, **635**, 931
- Byrd, G. G., Saarinen, S., & Valtonen, M. J. 1986, *MNRAS*, **220**, 619
- Chandrasekar, S. 1943, *ApJ*, **97**, 255
- Chiba, M., & Beers, T. C. 2000, *AJ*, **119**, 2843
- Colpi, M., Mayer, L., & Governato, F. 1999, *ApJ*, **525**, 720
- De Lucia, G. 2012, *AN*, **333**, 460
- Dehnen, W., & Binney, J. J. 1998, *MNRAS*, **298**, 387
- Dinescu, D. I. 2002, in *Ω Centauri: A Unique Window into Astrophysics*, Vol. 265, ed. F. van Leeuwen, J. Hughes, & G. Piotto (San Francisco, CA: ASP), 365
- Duffau, S., Vivas, K. A., Zinn, R., Mendez, R. A., & Ruiz, M. T. 2014, *A&A*, **566**, 118
- Eggen, O. J. 1971, *PASP*, **83**, 285
- Eggen, O. J. 1977, *ApJ*, **215**, 812
- Freeman, K., & Bland-Hawthorn, J. 2002, *ARA&A*, **40**, 487
- Gilmore, G., Randich, S., Asplund, M., et al. 2012, *Msngr*, **147**, 25
- Girardi, L., Grebel, E. K., Odenkirchen, M., & Chiosi, C. 2004, *A&A*, **422**, 205
- Gomez, F. A., Helmi, A., Cooper, A. P., et al. 2013, *MNRAS*, **436**, 3602
- Gould, A. 2003, *ApJL*, **592**, L63
- Harding, P., Morrison, H. L., Olszewski, E. W., et al. 2001, *AJ*, **122**, 1397
- Hastie, T., Tibshirani, R., & Friedman, J. 2001, *The Elements of Statistical Learning* (Berlin: Springer)
- Helmi, A. 2008, *A&AR*, **15**, 145
- Helmi, A., Cooper, A. P., White, S. D. M., et al. 2011, *ApJL*, **733**, L7
- Helmi, A., & de Zeeuw, P. T. 2000, *MNRAS*, **319**, 657
- Helmi, A., & White, S. D. M. 1999, *MNRAS*, **307**, 495
- Helmi, A., White, S. D. M., de Zeeuw, P. T., & Zhao, H. S. 1999, *Natur*, **402**, 53
- Hernquist, L. 1993, *ApJS*, **86**, 389
- Ibata, R. A., Gilmore, G., & Irwin, M. J. 1994, *Natur*, **370**, 194
- Ibata, R. A., Irwin, M. J., Lewis, G. F., Ferguson, A. M. N., & Tanvir, N. 2003, *MNRAS*, **340**, 21
- Ivezić, Ž., Sesar, B., Jurić, M., et al. 2008, *ApJ*, **684**, 287
- Johnston, K. V. 1998, *ApJ*, **495**, 297
- Kaufmann, L., & Rousseeuw, P. J. 1990, *Finding Groups in Data* (New York: John Wiley & Sons Inc.)
- Kepley, A. A., Morrison, H. L., Helmi, A., et al. 2007, *AJ*, **134**, 1579
- Klement, R., Rix, H.-W., Flynn, C., et al. 2009, *ApJ*, **698**, 865
- Klement, R. J. 2010, *A&AR*, **18**, 567
- Lasker, B. M., Lattanzi, M. G., McLean, B. J., et al. 2008, *AJ*, **139**, 735
- Lee, Y. S., Beers, T. C., Sivarani, T., et al. 2008a, *AJ*, **136**, 2022
- Lee, Y. S., Beers, T. C., Sivarani, T., et al. 2008b, *AJ*, **136**, 2050
- Majewski, S. R., Munn, J. E., & Hawley, S. L. 1996, *ApJ*, **459**, 73
- Majewski, S. R., Nidever, D. L., Smith, V. V., et al. 2012, *ApJL*, **747**, L37
- Meza, A., Navarro, J. F., Abadi, M. G., & Steinmetz, M. 2005, *MNRAS*, **359**, 93
- Moore, B., Diemand, J., Madau, P., Zemp, M., & Stadel, J. 2006, *MNRAS*, **368**, 563
- Morrison, H. L., Helmi, A., Sun, J., et al. 2009, *ApJ*, **694**, 130
- Munn, J. A., Monet, D. G., Levine, S. E., et al. 2008, *AJ*, **136**, 895
- Murante, G., Poggio, E., Curir, A., & Villalobos, A. 2010, *ApJL*, **716**, L115
- Navarrete, C., Chaname, J., Meza, A., et al. 2015, *ApJ*, **808**, 103
- Navarro, J. F., Frenk, C. S., & White, S. D. M. 1997, *ApJ*, **490**, 493
- Pasetto, S., Grebel, E. K., Zwitter, T., et al. 2012, *A&A*, **547**, A70
- Perryman, M. A. C., de Boer, K. S., Gilmore, G., et al. 2001, *A&A*, **369**, 339
- Re Fiorentin, P., Bailer-Jones, C. A. L., Lee, Y. S., et al. 2007, *A&A*, **467**, 1373
- Re Fiorentin, P., Helmi, A., Lattanzi, M. G., & Spagna, A. 2005, *A&A*, **439**, 551
- Read, J. I., Lake, G., Agertz, O., & Debattista, V. P. 2008, *MNRAS*, **389**, 1041
- Sales, L. V., Navarro, J. F., Abadi, M. G., & Steinmetz, M. 2007, *MNRAS*, **379**, 1464
- Schlafly, E. F., & Finkbeiner, D. P. 2011, *ApJ*, **737**, 103
- Schlafly, E. F., Green, G., Finkbeiner, D. P., et al. 2014, *ApJ*, **789**, 15
- Schlaufman, K. C., Rockosi, C. M., Allende Prieto, C., et al. 2009, *ApJ*, **703**, 2177
- Schlaufman, K. C., Rockosi, C. M., Lee, Y. S., Beers, T. C., & Allende Prieto, C. 2011, *ApJ*, **734**, 49
- Schlegel, D. J., Finkbeiner, D. P., & Davis, M. 1998, *ApJ*, **500**, 525
- Searle, L., & Zinn, R. 1978, *ApJ*, **225**, 357
- Smith, M. C., Evans, N. W., Belokurov, V., et al. 2009, *MNRAS*, **399**, 1223
- Spagna, A., Bucciarelli, B., Lattanzi, M. G., Re Fiorentin, P., & Smart, R. L. 2010b, *MemSAIt*, **14**, 67
- Spagna, A., Carollo, D., Lattanzi, M. G., & Bucciarelli, B. 2004, *A&A*, **428**, 451
- Spagna, A., Lattanzi, M. G., Re Fiorentin, P., & Smart, R. L. 2010a, *A&A*, **510**, L4
- Springel, V. 2005, *MNRAS*, **364**, 1105
- Starkenbourg, E., Helmi, A., Morrison, H. L., et al. 2009, *ApJ*, **698**, 567
- Trumpler, R. J., & Weaver, H. F. 1953, *Statistical Astronomy* (New York: Dover)
- Turon, C., O’Flaherty, K. S., & Perryman, M. A. C. (ed.) 2005, *The Three-dimensional Universe with Gaia* (ESA-SP, Vol. 576; Noordwijk: ESA)
- Villalobos, A., & Helmi, A. 2008, *MNRAS*, **391**, 1806
- Yanny, B., Rockosi, C., Newberg, H. J., et al. 2009, *AJ*, **137**, 4377
- Zhao, G., Zhao, Y.-H., Chu, Y.-Q., et al. 2012, *RAA*, **12**, 723